NANO LETTERS

LETTER

pubs.acs.org/NanoLett

# Electrical Transport Properties of Oligothiophene-Based Molecular Films Studied by Current Sensing Atomic Force Microscopy

Bas L. M. Hendriksen,[†,▽] Florent Martin,[†,‡] Yabing Qi,[†,○] Clayton Mauldin,[§] Nenad Vukmirovic,[†,◆] JunFeng Ren,[†,∥] Herbert Wormeester,[⊥] Allard J. Katan,[†] Virginia Altoe,[#] Shaul Aloni,[#] Jean M. J. Fréchet,[§] Lin-Wang Wang,[†] and Miquel Salmeron*[,†,‡]

[†]Materials Science Division, Lawrence Berkeley National Laboratory, Berkeley, California 94720, United States

[‡]Materials Science and Engineering Department, University of California Berkeley, Berkeley, California 94720, United States

[§]Department of Chemistry, University of California Berkeley, Berkeley, California 94720, United States

[∥]College of Physics and Electronics, Shandong Normal University, Jinan, 250014, China

[⊥]MESA+ Institute for Nanotochnology, Faculty of Science and Technology University of Twente, Enschede, The Netherlands

[#]The Molecular Foundry, Lawrence Berkeley National Laboratory, Berkeley, California 94720, United States

Supporting Information

**ABSTRACT:** Using conducting probe atomic force microscopy (CAFM) we have investigated the electrical conduction properties of monolayer films of a pentathiophene derivative on a $SiO_2$/Si-p+ substrate. By a combination of current−voltage spectroscopy and current imaging we show that lateral charge transport takes place in the plane of the monolayer via hole injection into the highest occupied molecular orbitals of the pentathiophene unit. Our CAFM data suggest that the conductivity is anisotropic relative to the crystalline directions of the molecular lattice.

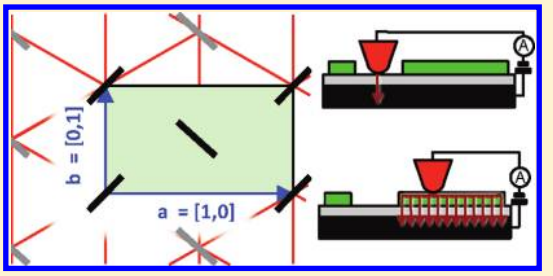


**KEYWORDS:** Oligothiophene, Langmuir−Blodgett monolayer, current sensing atomic force microscopy, molecular electronics, conduction anisotropy, lateral transport

The use of molecules as components of molecular scale electronic devices is a field of continuous interest, both in its fundamental scientific aspects and for potential applications in devices such as organic light emitting diodes and biosensors.[1−3] However, the electronic properties of the molecules and the correlation with their structure and assembly is still not well understood. Such understanding is necessary for the discovery of new properties and for the design of molecular scale devices. Efforts in that direction are underway in various laboratories. For example, intra- and intermolecular charge transport mechanisms have been studied in single molecules,[4] in molecular monolayers, in thin films,[5−8] in molecular crystals[9] and in biomolecular materials.[10]

Using conducting probe (current sensing) atomic force microscopy (CAFM) we investigated the electrical conduction properties of monolayer films of an oligothiophene derivative, 4-(5‴″-Decyl-[2,2′;5′,2″;5″,2‴;5‴,2‴″] pentathiophen-5-yl)-butyric acid, or D5TBA for short (Figure 1a). Oligo- and poly thiophenes are p-type semiconductors that have applications in electronic devices and photovoltaics.[11,12] The structural and mechanical properties of self-assembled monolayers of D5TBA and of a similar molecule, TD5TBA on mica, have been studied previously with AFM.[13−15]

In this work, we show how electric charge is transported over micrometer distances away from the point of injection in monolayer thin films of oligothiophene molecules. The experimental setup that made this study possible is an unconventional diode configuration, where one electrode (the Si-$p^+$ substrate) is covered by a thin insulating $SiO_2$ film and the other electrode is a conductive Pt-coated tip of an AFM. The $SiO_2$ film plays a crucial role because it prevents the conducting substrate from short-circuiting the molecules, effectively separating conduction channels through and across the molecules (Figure 1g). The current flowing laterally through the oligothiophene molecules is determined from the increase in tip-to-substrate current. In other words, we do not measure the current between the AFM tip and a laterally separated electrode;[8,16] instead the lateral transport is determined from its contribution to the current flowing from the CAFM tip and spreading through the molecular film before going to the substrate. We use CAFM to simultaneously determine the structure and the charge transport properties. CAFM has the advantage of preserving the structural integrity of the film, whereas contacting the molecular monolayers with microfabricated electrodes generally disrupts the layers.

**Structure of the D5TBA Monolayer.** The molecular films of D5TBA were prepared using the Langmuir−Blodgett (LB) technique. The typical morphology of D5TBA on native-$SiO_2$/

**Received:** May 17, 2011
**Revised:** August 17, 2011
**Published:** August 17, 2011

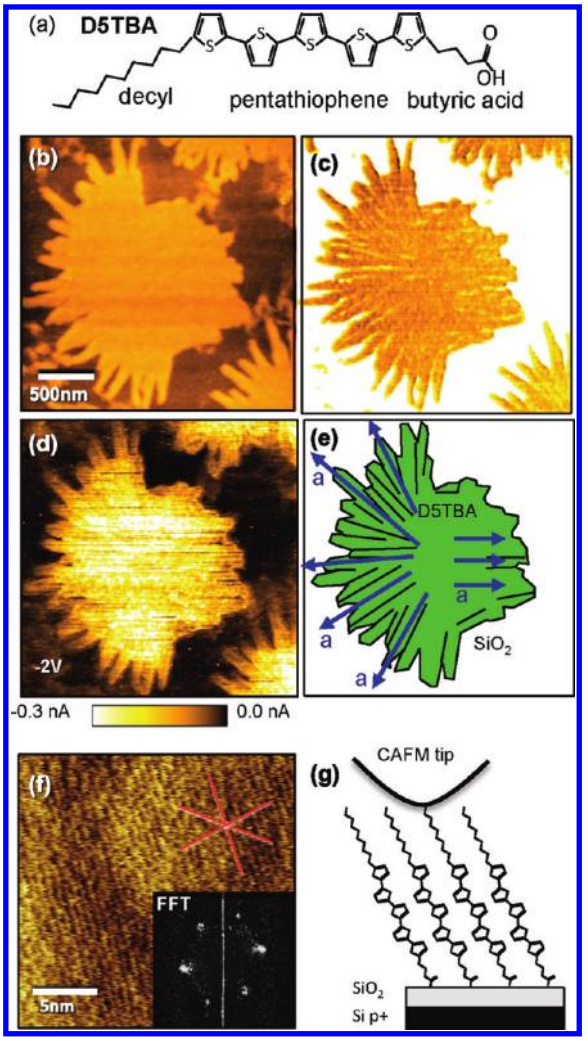


**Figure 1.** (a) Structure of the decyl-pentathiophene-butyric acid (D5TBA) molecule. (b) Topography of a characteristic monolayer island of D5TBA on $SiO_2$/Si. (c) Friction image, with dark corresponding to lower friction. (d) Image of the current measured at the tip at −2 V sample voltage. (e) Schematic representation of the D5TBA island. Black lines represent domain boundaries, blue arrows indicate the *a* direction of the molecular lattice (see Figure 2a). (f) Lattice-resolved friction image of one domain; red lines indicate the molecular lattice row directions in real space; the Fourier transform is shown in the inset. (g) Schematic of D5TBA molecules on a silicon substrate covered by the native oxide.

Si imaged by AFM is shown in Figure 1b,c. The film is always in the form of flowerlike islands with an island−island separation determined by the surface pressure during emersion of the sample from the LB trough. The height of the islands is 2.5 nm, which is smaller than 3.65 nm expected for fully extended molecules. The friction force on the islands is always lower than on the substrate (Figure 1c) due to the inert and lubricating properties of the exposed alkane chains. The size of the island varies from hundreds to thousands of nanometers. They are composed of elongated fingerlike domains extending roughly radially from the center as a result of nucleation from a point close to the center (Figure 1e). The domains are separated by boundaries that are particularly visible in friction images by the larger value of the force as the tip scans over them (Figure 1c).

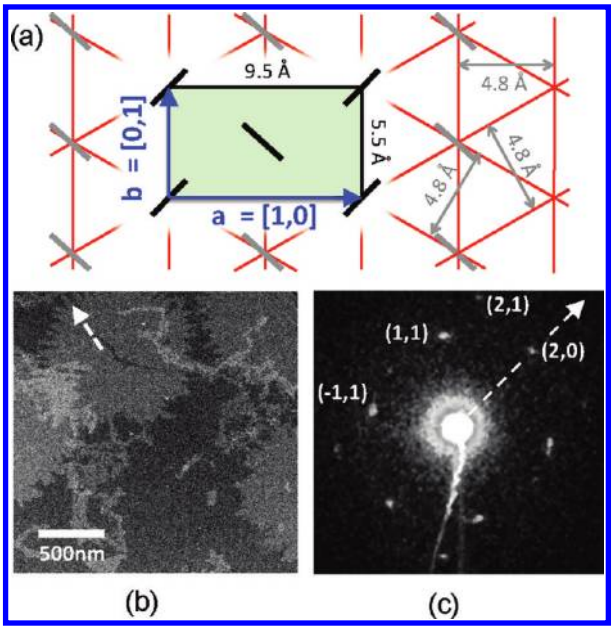


**Figure 2.** (a) Schematic top view of the Herringbone structure. Red lines represent directions where the molecules are most closely packed. These are the lattice rows resolved in the AFM images. Black and grey segments represent the thiophene units (b) TEM image of islands on a SiN substrate. The arrow indicates the *a* direction of the lattice in real space on the fingerlike domain where the diffraction pattern (c) was recorded. (c) TEM diffraction pattern. Notice the absence of (1,0) and (0,1) diffraction spots. The *a* direction in reciprocal space is shown by the arrow.

This is consistent with the general observation that structural disorder gives rise to higher friction.[17] The CAFM current image shown in Figure 1d was recorded simultaneously with Figure 1b,c and will be discussed below.

Figure 1f shows a lattice resolved AFM friction image from one domain of the D5TBA islands on the $SiO_2$/Si substrate. The Fourier transform of the image (inset in Figure 1f) shows a nearly hexagonal symmetry. We found that D5TBA films deposited on mica have the same morphology and structure as D5TBA on $SiO_2$/Si substrates. Lattice-resolved images of the mica substrate obtained in the same experiment were used as a reference to correct for image distortions due to thermal drift and nonlinearity of the piezo scanner. In this way, the spacing between rows of molecules was measured to be 4.8 ± 0.4 Å and the angle between lattice directions 60 ± 5°. Such an apparent hexagonal lattice is consistent with the well-known Herringbone structure commonly found for planar $\pi$-systems.[5]

In the AFM experiments, the AFM tip is in contact with the alkyl chains and the orientation of the thiophene rings is not visible. This and the fact that we measure similar row spacings of 4.8 Å for each direction prevents us from unambiguously indexing the lattice directions in the images. To obtain more information on the structure of the unit cell we used electron diffraction in a transmission electron microscope (Figure 2). In this experiment, monolayers of D5TBA were deposited on hydrophilic SiN TEM windows using the LB method. As shown in Figure 2b, the morphology of the islands is the same as on the $SiO_2$/Si and mica substrates. The diffraction pattern shown in Figure 2c was acquired with a beam size of 100 nm through an individual fingerlike domain (arrow in Figure 2b) and shows


dx.doi.org/10.1021/nl202720y |*Nano Lett.* 2011, 11, 4107–4112

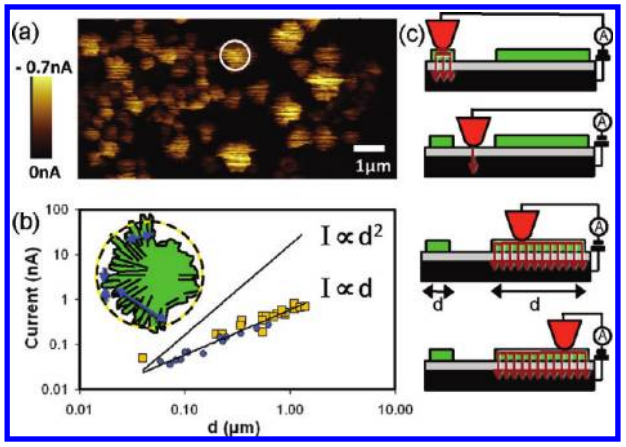


**Figure 3.** (a) Current-sensing AFM image of D5TBA monolayer islands on a $SiO_2$/Si-p+ substrate at $V_{sample} = -2.0$ V. (b) Dependence of the current on average island diameter (yellow squares) and on the local width in the *b* lattice direction (blue circles) within islands. Diameter and width are defined in the inset by the yellow circle and the blue arrows. (c) Schematic representation of the AFM-sample contact. On the bare $SiO_2$/Si substrate current only flows through the $SiO_2$ in the contact area of the tip. Over the islands the current can flow laterally over a distance *d*, before tunneling through the $SiO_2$. This gives rise to the island size dependence.

strong (−1,1), (1,1), (2,0), and (2,1) reflections. The conspicuous absence of (1,0) and (0,1) reflections is the result of glide reflection symmetry in the *p2gg* space group, consistent with the Herringbone structure of the unit cell of the D5TBA film (Figure 2a).

We also performed classical molecular dynamics calculations to determine the most stable packing of the D5TBA molecules. We have tested the CFF91 force field,[18] as implemented in the LAMMPS code,[19] as well as the COMPASS force field.[20] We found a better agreement for the COMPASS force field with the experimental results. We have thus rescaled the Lennard-Jones parameter $\sigma$ by 87% in the CFF91 force field to match the results of the COMPASS force field. This allows us to calculate large systems with the LAMMPS code. Various initial structures and lattice constants were explored. The lowest energy configuration after relaxation is indeed a Herringbone structure (Figure 2a) with the D5TBA molecules inclined to give a film height of 2.7 nm (Figure 1g). The calculated unit cell dimensions are $a$ = 9.5 Å in the [1,0] direction and $b$ = 5.5 Å in the [0,1] direction. The lines in Figure 2a are drawn along directions of close molecular packing, which correspond to the rows resolved in AFM: two equivalent diagonal directions and a third direction parallel to [0,1]. The spacing between parallel rows of 4.8 Å is in agreement with the periodicity measured in the AFM images. The structure measured by electron diffraction is similar to the calculated one with a unit cell that was only slightly different ($a$ = 9.1 ± 0.4 Å, $b$ = 5.9 ± 0.3 Å). Whether this small discrepancy is due to substrate−monolayer interactions is currently under investigation.

We measured the orientation of the long axis in the fingerlike domains relative to the directions of the molecular lattice in both AFM and TEM. AFM images of adjacent domains of D5TBA monolayer on mica revealed that the molecular lattice had a fixed orientation relative to the fingerlike domain short axis with one lattice row direction being always orthogonal to the long axis of the domains. The same comparison was done with TEM from which we conclude that the $a$ = [1,0] and $b$ = [0,1] directions of the unit cell are respectively parallel (as shown in Figure 1e) and orthogonal to the long axis of domains (see Supporting Information Figure S1).

**Lateral Charge Transport and Anisotropy.** The electrical conduction properties of the D5TBA islands were studied using CAFM. A net load of 15 nN was applied for a reliable electrical contact without noticeable perturbation of the molecules. Much higher loads however do affect the current, an interesting effect that will be described separately in a forthcoming paper. Typical current images are shown in Figures 1d, 3a, and 6a,b. The current level at each pixel of the CAFM current image is the combined result of (1) injection of charge carriers from the tip (substrate) into the monolayer island, (2) transport through the monolayer island, and (3) ejection from the monolayer island into the substrate (tip). The first observation is that for negative sample bias the current is higher on the islands than on the bare $SiO_2$. This seems counterintuitive: by adding material and increasing the separation between the metallic tip and the substrate by 2.5 nm, the resistance of the junction decreases. In principle, the addition of an organic layer in the junction can increase the tip−sample current by modifying the potential drop in the junction.[21] However, here we demonstrate that the higher current level on the islands is due to lateral conduction across molecules, which increases the effective electrical contact area.

Current images, as those in Figures 3a and 6a, show that at negative sample voltage the current level is significantly higher on the larger islands. Figure 3b shows a log−log plot of the average current for each island as a function of the island size at $V_{sample}$ = −2 V. The current increases linearly with island size up to several micrometers in the largest islands. The lattice periodic structure, thickness of the monolayer, tip−sample contact potential difference (CPD, not shown here), tip load, and the thickness of the $SiO_2$ are the same for all island sizes, although they may vary locally within an island. Therefore we do not expect that the barriers for injection and ejection of charge carriers in and out of the islands vary with island size. Instead, we propose that the island size dependence of the current at negative sample voltage is the result of charge carrier transport laterally through the monolayer (Figure 3c).

Lateral transport in SPM junctions containing nanometer-size clusters of molecules was first demonstrated by STM measurements of the apparent height as a function of cluster size.[22−24] CAFM provides a more direct method to determine conductivity properties, since the tip−sample distance is controlled independently of the transport current.[25,26] Lateral conduction in a molecular film can become significant if the barrier for carrier transport from molecule to molecule is small compared to the barrier between molecule and substrate. This can be illustrated by a resistor network (see Figure 4c), where N + 1 parallel resistors represent the intermolecule resistances ($R_{mol\text{-}mol}$). Each of the molecules is connected to the substrate by a series resistance ($R_{mol\text{-}sub}$). This leads to a reduction of the total resistance of the junction for the 1D case as $1/R = (1/R_{mol-sub}) + \Sigma_{n=1}^{N}(2/R_{mol-sub} + nR_{mol-mol})$.[22−24] From this it is easy to see that it is thanks to the thin insulating $SiO_2$ layer that the lateral intermolecular charge transport can be clearly observed in our measurements, that is, $R_{mol\text{-}sub}$ is large compared to $R_{mol\text{-}mol}$. On a substrate without oxide barrier, for example, Au, the vertical transport through the D5TBA molecules is dominant. We should emphasize that an ohmic resistor model does not realistically represent the true transport properties of the molecules and


dx.doi.org/10.1021/nl202720y |*Nano Lett.* 2011, 11, 4107–4112

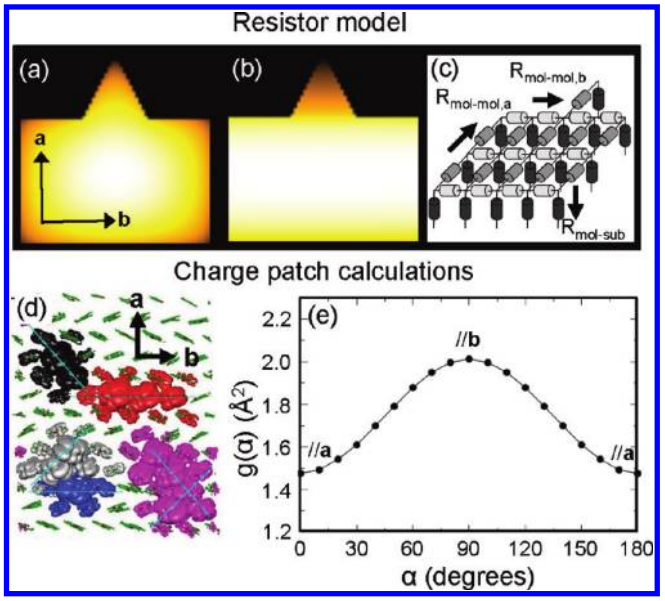


**Figure 4.** Conduction anisotropy in resistor model and charge patch calculations. (a,b) Calculated current images for a simplified island geometry consisting of a square main body and a fingerlike protrusion using a resistor network. (a) isotropic conduction model, where $R_{mol-mol,a} = R_{mol-mol,b}$. (b) Anisotropic conduction model where $R_{mol-mol,a} > R_{mol-mol,b}$. (c) Resistor network consisting of resistors $R_{mol-mol,a}$ and $R_{mol-mol,b}$ representing the contact resistance between molecules in the *a* and *b* directions, and $R_{mol-sub}$ representing the molecule−substrate contact resistance (for clarity only a small network is shown). (d) Top five hole wave functions corresponding to a snapshot in a room temperature molecular dynamics simulation of the 7 × 7 cell Herringbone structure. The globular shapes are isosurfaces enclosing regions with 98% probability of finding the hole inside. The energies of the five levels are 2.787 (blue), 2.758 (red), 2.746 (pink), 2.738 (black), 2.735 eV (gray). (e) Plot of g (proportional to carrier mobility) as a function of the angle α in the unit cell, with 90° corresponding to the *b* = [0,1] direction.

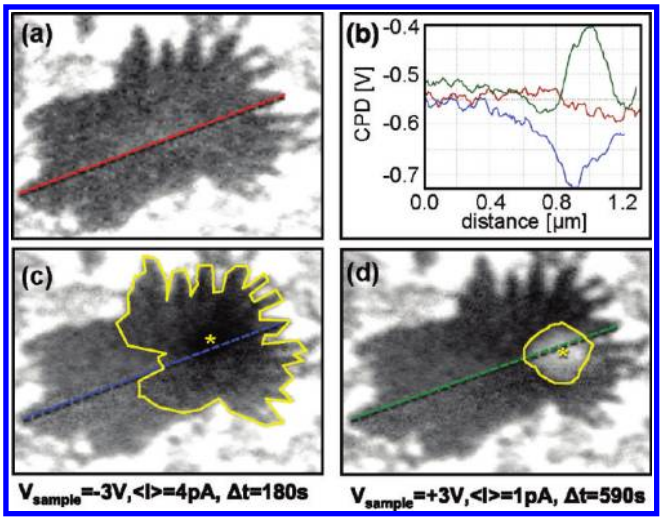


**Figure 5.** (a,c,d) Kelvin probe microscopy images of the contact potential difference (CPD) between the Pt AFM tip and a D5TBA island (image size = 1.48 × 1.20 μm, NC-AFM parameters: *f* = 68kHz, Δ*f* = −30 Hz. KPFM sample voltage modulation: frequency $f_{KPFM}$ = 1.2kHz, amplitude $A_{KPFM}$ = 0.05 V). (b) Line profiles of the CPD along the lines in each image (see also Supporting Information). Between (a) and (c) the monolayer was point contacted by the tip at the position marked * at a $V_{sample}$ = −3 V. This resulted in a lowering of the CPD in an area well outside of the tip-island contact. Between (c) and (d) the island was point contacted at $V_{sample}$ = +3 V resulting in an increase in the CPD. Yellow lines mark the boundaries of modified contact potential.

the tunneling barriers of our tip−molecular island−substrate junctions.

The graph in Figure 3b shows that the current scales linearly rather than quadratically with island diameter. This demonstrates that the current level is not simply proportional to the island area. It also suggests that the conduction is not isotropic. In order to relate the lateral conduction to the structure of the molecular lattice, we focus on the single-domain, fingerlike protrusions of the islands. We observe that the current level increases from the end of the fingerlike protrusions toward the island main body. The current gradient is not continuous but increases by steps when individual fingerlike domains or clusters of fingers connect (this can be observed in Figures 1d and 6a). To quantify these observations, we determined the dependence of current on local width of the domains in the *b* = [0,1] direction, that is, in the direction orthogonal to a finger long axis (which points in the *a*-direction). This direction is indicated by blue arrows in the inset of Figure 3b. The data in Figure 3b (blue dots) show that the current scales linearly with local width, which implies that the current is dominated by conduction pathways in the *b* = [0,1] direction of the domains. To further evaluate the effect of conduction anisotropy we calculated current images for a simplified island shape for isotropic and anisotropic conduction (Figure 4a,b) using a 2D resistor network model (Figure 4c) (see Supporting Information). For an isotropic resistor network the gradients in the current vary smoothly in all directions, while the anisotropic network reproduces better the characteristic gradients of the protrusions of the experimental CAFM current images. These results suggest that transport occurs preferentially in the *b* direction, where the thiophene rings of adjacent molecules are parallel to each other.

We used molecular dynamics simulations in a periodic 7 × 7 supercell of D5TBA to gain a molecular level insight on the dependence of conductivity on crystal lattice direction. We calculated the hole wave functions and their overlap at room temperature to estimate the anisotropy of the hole mobility. The calculation was performed using the charge patch method,[27] which has an accuracy similar to that of density functional theory in the local density approximation. A snapshot of the top five hole wave functions is shown in Figure 4d. The hole hopping probability between states *k* and *m* is assumed to be proportional to the square of the wave function moduli overlap

$$W_{km} \propto M_{km}^2 = [\int |\psi^{(k)}(\mathbf{r})||\psi^{(m)}(\mathbf{r})|d^3\mathbf{r}]^2$$

where $\psi^{(k)}$ and $\psi^{(m)}$ are the wave functions for the room-temperature structure (not the ideal zero temperature crystal one), which are obtained from snapshots in the molecular dynamics simulation. In recent work,[28] we have shown that such overlap integral approximates very well the full hopping matrix calculated by taking into account the electron−phonon interaction.

The function *g*, defined as

$$g(\alpha) = \langle[(x_k - x_m)\cos\alpha + (y_k - y_m)\sin\alpha]^2 M_{km}{}^2\rangle$$

is proportional to the diffusion constant and to the carrier mobility by the Einstein relation (see the Supporting Information


dx.doi.org/10.1021/nl202720y |*Nano Lett.* 2011, 11, 4107–4112

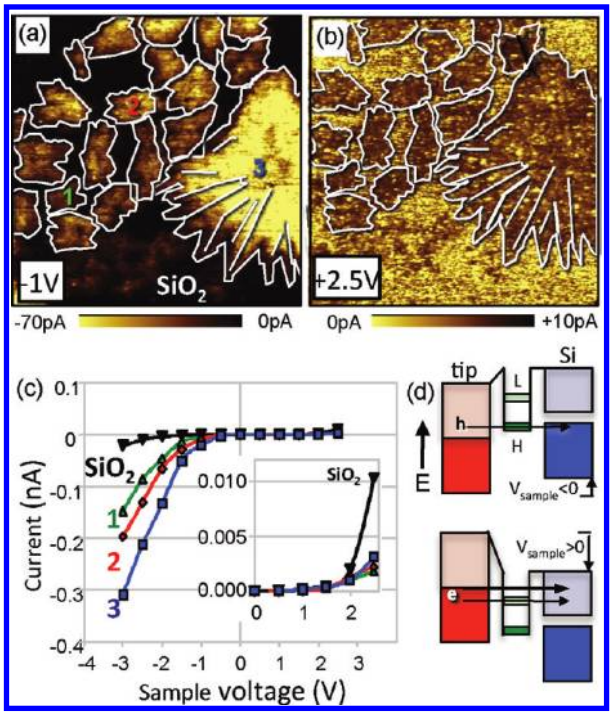


**Figure 6.** (a) current image at $V_{sample}$ = −1.0 V, (b) current image at $V_{sample}$ = +2.5 V of D5TBA on $SiO_2$/Si in dry $N_2$. The outline of the D5TBA islands has been superimposed (see Supporting Information for more details). (c) Current−voltage spectra acquired in the four locations marked in (a). The current is obtained by averaging selected regions of the islands. (d) Schematic energy diagram of charge transport through the tip−molecular island−$SiO_2$−Si junction. For $V_{sample}$ < 0, holes are injected in the HOMOs of the molecules contacted by the tip. Holes move laterally through the islands across HOMO (H) orbitals of adjacent molecules followed by tunneling through the $SiO_2$. For $V_{sample}$ > 0 transport results mainly from direct tunneling with a small contribution by lateral transport through the LUMO (L) levels.

for more details). This function quantifies the angular dependence of hole mobility. In Figure 4e, we plot the dependence of $g$ on the direction α. The hole mobility is 30% larger in the $b$ = [0,1] direction than in the $a$ = [1,0] direction, which is in qualitative agreement with our experimental results.

An additional proof for lateral transport is provided by Kelvin probe force microscopy (KPFM), which makes possible to detect local potential distribution due to local dipoles and trapped charges, which we could locally introduce by tip contact at sufficiently high voltages.[29] Figure 5a shows a KPFM image of an island, which appears more negative than the surrounding substrate relative to the tip. The island was subsequently contacted by the tip at the locations marked by a star in (c) and (d), first at $V_{sample}$ = −3 V sample bias (Figure 4c) and later at $V_{sample}$ = +3V (Figure 4d) (see Supporting Information). After contact at $V_{sample}$ = −3 V, positive charges became trapped, while after contact at $V_{sample}$ = +3 V the trapped charges were negative. The amount of trapped charge increased with the duration of the current flow. The measurements however do not provide information on the location of the trapped charges, that is, in the D5TBA island or in the underlying $SiO_2$. The results however show that they can be found well outside of the CAFM tip contact area of 50 nm, again showing that charge carriers injected into the molecular islands move laterally. We note that the probability of charge trapping was low, so that measurable effects on the current images were only visible after prolonged current flow, much longer than that required to acquire a series of CAFM current images.

**Electronic Properties of the D5TBA Monolayer.** The electronic properties of the D5TBA islands and of the exposed $SiO_2$ substrate were studied by current−voltage ($I$−$V$) spectroscopy. $I$−$V$ spectra were obtained by averaging the current over selected regions in images acquired at sample bias between −3 V and +2.5 V in 0.5 V increments (Figure 6a,b). The $I$−$V$ curves of the Pt−$SiO_2$−Si junction (acquired on the bare substrate regions) are consistent with tunneling through the oxide with no rectifying effect. The doping level of the silicon is such that it can be considered as a metal. In contrast, $I$−$V$ curves acquired over the islands show a rectifying behavior. For negative sample voltages the current onset is close to −0.5 V, while for positive voltages the onset is close to +2.0 V. Curves 1, 2, and 3 correspond to the islands marked with the corresponding numbers in Figure 6a. The curves have the same dependence but scale according to their size. The images in Figure 6a,b were acquired at $V_{sample}$ = −1.0 V and +2.5 V, which are 0.5 V below and above the current onsets for negative and positive sample biases (for the complete set see Supporting Information).

The rectifying behavior of a molecular junction[30] can be caused for example by Aviram-Ratner donor−acceptor moieties,[31] asymmetric tunneling barriers,[32−34] Schottky barriers,[35] and pinning of the electronic levels at the molecule/substrate interface.[36] The observed asymmetry of the current shown in Figure 6c is best explained by pinning of the molecular orbitals to the Si substrate Fermi level. Pinning leads to well-defined voltages at which injection of electrons and holes into the lowest unoccupied molecular orbitals (LUMO) and the highest occupied molecular orbitals HOMO respectively becomes efficient (Figure 6d).[37] Pinning to the substrate despite the interposed oxide film can be rationalized first by the strong bond between the butyric acid headgroup and the substrate, as compared to the weak van der Waals interaction between the tip and the methyl end groups of the alkyl chains. Second, the high lateral conductivity of the monolayer effectively enhances the contact area between the thiophene part of the molecular film and the Si substrate.

Unsubstituted oligothiophenes are p-type semiconductors with the HOMO at 4 to 5.5 eV below the vacuum level, which is close to both the Fermi level of Pt on the tip and of the Si.[11] We therefore conclude that the lateral conduction at negative sample voltage is through the HOMO orbitals located approximately 0.5 V below the sample Fermi level (Figure 6e). This agrees with the observation of trapped positive charge (holes, after a conduction measurement at negative sample voltage (Figure 5c). At positive sample bias, the current increases only above +2 V but remains well below the value measured in the tip−$SiO_2$−Si contacts outside the islands. KPFM demonstrated that at $V_{sample}$ = +3 V at least some electrons were injected in the monolayer islands and that these were transported laterally. Two observations, however, suggest that the lateral electron transport does not contribute substantially to the tip−sample current at positive sample bias; the current image of an island is virtually independent of island size and is not homogeneous, showing strong local spikelike variations (see also Supporting Information). Lateral transport would smear out such local current variations, as observed for negative sample voltages. Therefore only limited lateral transport occurs if an electron is injected into the LUMO. The electron tunnels into the oxide more effectively than hopping to a neighboring molecule. Therefore we ascribe the


dx.doi.org/10.1021/nl202720y |Nano Lett. 2011, 11, 4107–4112

smaller current at positive sample voltages to a much-reduced lateral mobility of the electrons, possibly in combination with a reduced efficiency for electron injection in the LUMO. Mechanisms that could account for a reduced mobility include recombination and scattering by holes in the HOMO or a high density of trap states for electrons.[37]

**Conclusions.** The structure of decyl-pentathiophene butyric acid (D5TBA) islands on various substrates ($SiO_2$/Si, mica and SiN TEM supports) has been determined by a combination of AFM topographical and friction imaging, transmission electron microscopy, as well as molecular dynamics calculations. The presence of an insulating oxide film between the D5TBA molecules and the Si substrate electrode made possible the study of lateral conduction, which led to a linear island size dependence of the CAFM tip−substrate current. The electrical properties of the film on $SiO_2$/Si were investigated by $I-V$ spectroscopy. A strong rectifying behavior was observed with the current being 2 orders of magnitude higher at negative sample voltage, which involves the HOMO orbitals, than at positive voltage. Conduction through the HOMO orbitals increases with island size up to 1.5 $\mu$m and shows clear signs of anisotropy with higher conductivity orthogonal to the domain growth direction, which corresponds to the direction where $\pi$-orbitals of the thiophene units overlap more strongly. Our study provides a clear link between the molecular level orbital structure, crystallography, and electronic properties of the films.

## ■ ASSOCIATED CONTENT

**Supporting Information.** Additional information and figures. This material is available free of charge via the Internet at http://pubs.acs.org.

## ■ AUTHOR INFORMATION


### Corresponding Author

*E-mail: MBSalmeron@lbl.gov.

### Present Addresses

[▽]Institute for Molecules and Materials, Radboud University, 6525 AJ Nijmegen,The Netherlands.

[○]Department of Electrical Engineering, Princeton University, Princeton, New Jersey 08544.

[◆]Scientific Computing Laboratory, Institute of Physics Belgrade, University of Belgrade, Pregrevica 118, 11080 Belgrade, Serbia.


## ■ ACKNOWLEDGMENT

This work was supported by the Office of Science, Office of Basic Energy Sciences, Materials Science and Engineering of the U.S. Department of Energy under Contract No. DE-AC02-05CH11231. V.A. and S.A. are supported by the Molecular Foundry, Lawrence Berkeley National Laboratory. The simulations were performed using the resources of National Energy Research Scientific Computing Center (NERSC).

## ■ REFERENCES


(1) Forrest, S. R. *Nature* **2004**, *428*, 911–918.

(2) Joachim, C.; Gimzewski, J. K.; Aviram, A. *Nature* **2000**, *408*, 541–548.

(3) Holmlin, R. E.; Haag, R.; Chabinyc, M. L.; Ismagilov, R. F.; Cohen, A. E.; Terfort, A.; Rampi, M. A.; Whitesides, G. M. *J. Am. Chem. Soc.* **2001**, *123*, 5075–5085.

(4) Xu, B. Q.; Tao, N. J. *J. Science* **2003**, *301*, 1221–1223.

(5) Smits, E. C. P.; Mathijssen, S. G. J.; van Hal, P. A.; Setayesh, S.; Geuns, T. C. T.; Mutsaers, K.; Cantatore, E.; Wondergem, H. J.; Werzer, O.; Resel, R.; Kemerink, M.; Kirchmeyer, S.; Muzafarov, A. M.; Ponomarenko, S. A.; de Boer, B.; Blom, P. W. M.; de Leeuw, D. M. *Nature* **2008**, *455*, 956–959.

(6) Dimitrakopoulos, C. D.; Malenfant, P. R. L. *Adv. Mater.* **2002**, *14*, 99.

(7) Yang, H. C.; Shin, T. J.; Ling, M. M.; Cho, K.; Ryu, C. Y.; Bao, Z. N. *J. Am. Chem. Soc.* **2005**, *127*, 11542–11543.

(8) Kelley, T. W.; Granstrom, E. L.; Frisbie, C. D. *Adv. Mater.* **1999**, *11*, 261.

(9) Gershenson, M. E.; Podzorov, V.; Morpurgo, A. F. *Rev. Mod. Phys.* **2006**, *78*, 973–989.

(10) Moser, C. C.; Keske, J. M.; Warncke, K.; Farid, R. S.; Dutton, P. L. *Nature* **1992**, *355*, 796–802.

(11) Murphy, A. R.; Frechet, J. M. *J. Chem. Rev.* **2007**, *107*, 1066–1096.

(12) Coakley, K. M.; McGehee, M. D. *Chem. Mater.* **2004**, *16*, 4533–4542.

(13) Chen, J. Y.; Murphy, A. R.; Esteve, J.; Ogletree, D. F.; Salmeron, M.; Frechet, J. M. *J. Langmuir* **2004**, *20*, 7703–7710.

(14) Ratera, I.; Chen, J.; Murphy, A.; Ogletree, D. F.; Frechet, J. M. J.; Salmeron, M. *Nanotechnology* **2005**, *16*, S235–S239.

(15) Chen, J.; Ratera, I.; Murphy, A.; Ogletree, D. F.; Frechet, J. M. J.; Salmeron, M. *Surf. Sci.* **2006**, *600*, 4008–4012.

(16) Kelley, T. W.; Frisbie, C. D. *J. Phys. Chem. B* **2001**, *105*, 4538–4540.

(17) Salmeron, M. *Tribol. Lett.* **2001**, *10*, 69–79.

(18) Hwang, M. J.; Stockfisch, T. P.; Hagler, A. T. *J. Am. Chem. Soc.* **1994**, *116*, 2515–2525.

(19) Plimpton, S. *J. Comput. Phys.* **1995**, *117*, 1–10.

(20) Sun, H. *J. Phys. Chem. B* **1998**, *102*, 7338–7364.

(21) Yan, H. J.; McCreery, R. L. *ACS Appl. Mater. Interfaces* **2009**, *1*, 443–451.

(22) Ishida, T.; Mizutani, W.; Akiba, U.; Umemura, K.; Inoue, A.; Choi, N.; Fujihira, M.; Tokumoto, H. *J. Phys. Chem. B* **1999**, *103*, 1686–1690.

(23) Yokota, Y.; Fukui, K.; Enoki, T.; Hara, M. *J. Am. Chem. Soc.* **2007**, *129*, 6571–6575.

(24) Kafer, D.; Bashir, A.; Dou, X.; Witte, G.; Mullen, K.; Woll, C. *Adv. Mater.* **2010**, *22*, 384–+.

(25) Fang, L.; Park, J. Y.; Ma, H.; Jen, A. K. Y.; Salmeron, M. *Langmuir* **2007**, *23*, 11522–11525.

(26) Qi, Y. B.; Liu, X. S.; Hendriksen, B. L. M.; Navarro, V.; Park, J. Y.; Ratera, I.; Klopp, J. M.; Edder, C.; Himpsel, F. J.; Frechet, J. M. J.; Haller, E. E.; Salmeron, M. *Langmuir* **2010**, *26*, 16522–16528.

(27) Vukmirovic, N.; Wang, L. W. *J. Phys. Chem. B* **2009**, *113*, 409–415.

(28) Vukmirovic, N.; Wang, L. W. *Appl. Phys. Lett.* **2010**, *97*, 043305.

(29) Heim, T.; Lmimouni, K.; Vuillaume, D. *Nano Lett.* **2004**, *4*, 2145–2150.

(30) Metzger, R. M. *Chem. Rev.* **2003**, *103*, 3803–3834.

(31) Aviram, A.; Ratner, M. A. *Chem. Phys. Lett.* **1974**, *29*, 277–283.

(32) Datta, S.; Tian, W. D.; Hong, S. H.; Reifenberger, R.; Henderson, J. I.; Kubiak, C. P. *Phys. Rev. Lett.* **1997**, *79*, 2530–2533.

(33) Kornilovitch, P. E.; Bratkovsky, A. M.; Williams, R. S. *Phys. Rev. B* **2002**, *66*, 165436.

(34) Krzeminski, C.; Delerue, C.; Allan, G.; Vuillaume, D.; Metzger, R. M. *Phys. Rev. B* **2001**, *64*, 085405.

(35) Liu, Y. Q.; Xu, Y.; Zhu, D. B. *Synth. Met.* **1997**, *90*, 143–146.

(36) Lenfant, S.; Guerin, D.; Van, F. T.; Chevrot, C.; Palacin, S.; Bourgoin, J. P.; Bouloussa, O.; Rondelez, F.; Vuillaume, D. *J. Phys. Chem. B* **2006**, *110*, 13947–13958.

(37) Chua, L. L.; Zaumseil, J.; Chang, J. F.; Ou, E. C. W.; Ho, P. K. H.; Sirringhaus, H.; Friend, R. H. *Nature* **2005**, *434*, 194–199.

# SUPPORTING INFORMATION

## Electrical transport properties of oligothiophene-based molecular films studied by current sensing Atomic Force Microscopy

Bas L. M. Hendriksen, Florent Martin, Yabing Qi, Clayton Mauldin, Nenad Vukmirovic, JunFeng Ren, Herbert Wormeester, Allard J. Katan, Virginia Altoe, Shaul Aloni, Jean M. J. Fréchet, Lin-Wang Wang and Miquel Salmeron*

**Experimental details**

The D5TBA oligomer was synthesized by Stille cross-coupling methods. The semiconducting part of the molecule is the pentathiophene unit (5T). The butyric acid group (BA) serves as a hydrophillic anchoring group and the hydrophobic decyl group ($C_{10}H_{21}$) improves solubility and promotes ordering. Monolayers of D5TBA were prepared by the Langmuir-Blodgett method. A volume of 1 ml of 0.1mM D5TBA in chloroform was deposited on the surface of ultrapure water contained in a Teflon trough. After evaporation of the chloroform the amphiphillic molecular layer floating on the water was compressed to surface pressures in the range of 0-10mN/m before deposition. The substrates were mica and p-type Si(001) wafers with a resistivity <0.00099 Ohm.cm covered by a native oxide 2.2 nm thick, as determined by ellipsometry. No qualitative differences were observed in the structural and electrical properties of D5TBA films on Si samples covered by native off-the-shelf oxide, or by oxides prepared by oxidation in acidic piranha solution, or in pure oxygen plasma. The D5TBA covered samples were heated to 90-100$^{o}$C for several hours in a $N_2$ atmosphere to remove water.

AFM images were obtained using a 5500 Agilent AFM in contact mode in a dry nitrogen atmosphere. For high-resolution contact-mode imaging, BudgetSensors 0.27N/m SiNi probes were used. Current imaging and I-V spectroscopy were performed using 0.2N/m Pt-coatedBudgetSensors ElectriCont-E probes. The p-type Si(001) sample was electrically contacted to the voltage supply by a spring-loaded copper wire. A net load of 15nN was applied for a reliable electrical contact without noticeable perturbation of the molecules.

TEM experiments were performed in a Jeol 2100F at 120kV on Langmuir-Blodgett D5TBA monolayers deposited on a silicon nitride membrane. The membrane was previously treated in oxygen plasma to make it hydrophilic. Electron diffraction patterns of single crystal domains were obtained using a collimated parallel illumination, with a spot size of approx. 100nm and corresponding flux of 10 electrons $Å^{-2}$ $s^{-1}$. To minimize the electron dose received by the organic monolayer, the beam was scanned with a step size of 100nm and dwell time of less than a second per pixel. More than one pattern was recoded at each pixel, each of them with an exposure of about 0.2 seconds. Scanning transmission electron micrographs such as fig.2 (main text) were recorded after the acquisition of the diffraction data. The rotation between the real space image and the diffraction patterns was taken into account and corrected for.

Kelvin Probe Force Microscopy (KPFM) was performed in a UHV environment at a pressure of $5 \cdot 10^{-9}$ Torr. The cantilevers were Pt-coated doped Si with spring constant and resonance frequency of 2 N/m and 75 kHz respectively (BudgetSensors Multi75E). We used single-pass imaging, i.e. topographical and contact potential images were obtained simultaneously, with the electrical modulation applied at a frequency far below the resonance frequency of the cantilever. Topograhical feedback was done in frequency modulation, non-contact mode. For the current spreading experiments, the tip was brought into controlled contact with the monolayer only for the duration of the current injection.

**Orientation of the domains**

In order to establish a relation between the structure of the molecular lattice and the island morphology we imaged the molecular lattice at high resolution with AFM on different areas of a D5TBA island, in particular on the finger-like protrusions, which are single-domain grains. In addition we recorded TEM diffraction patterns on various locations on an island. The result of this analysis is summarized by figure S1, which shows the correlation between α, the angle of the long axis of the grains with respect to a constant reference direction and β, the angle between the **a**=[1,0] direction of the molecular lattice and the same reference direction. The one-to-one correspondence indicates that the [1,0] direction is always parallel to the grain's long axis and consequently the **b**=[0,1] direction of the lattice is perpendicular to the long axis.

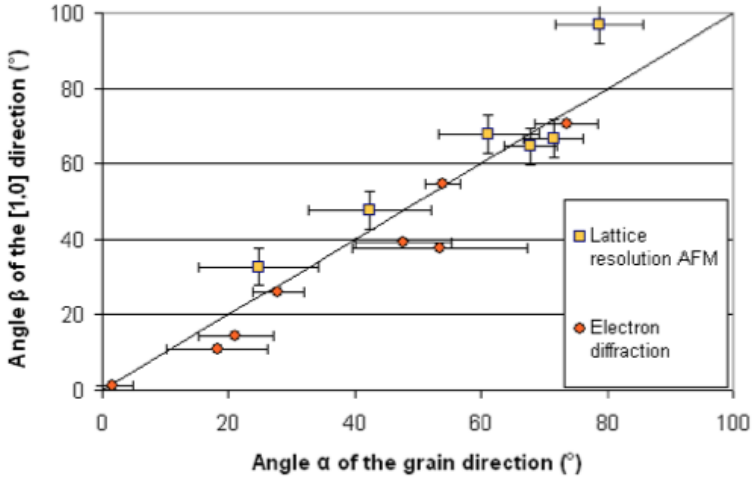


**Figure S1.** Scatter plot of domains long axis direction versus direction of the a molecular lattice vector [1,0] obtained for single grains by electron diffraction (orange circles), and lattice resolution AFM (yellow squares). The angles α and β are with respect to the same reference direction. The line α=β shows that the long axis of the domains is always parallel to the **a**=[1,0] lattice direction.

**Resistor model for anisotropy in lateral transport**

Figure 3 (main text) shows that the average current level of an island depends linearly on the size, given by the island diameter. We model this by a 1D and by a 2D network of Ohmic resistors, from which we derive the following relation:

$$I = \sum_{N} i_n = \frac{V}{R_{mol-sub}} + \sum_{n=1}^{N} 2\frac{V}{R_{mol-sub} + nR_{mol-mol}} \quad \text{(for the 1D case)}$$

Of course this linear approximation of the current dependence on the voltage does not represent the realistic characteristics of the intermolecular and molecule-substrate transport.

Figure S2 shows conduction maps of a circular island where for each pixel the current contributions are calculated for the 1D and for the 2D cases. The distance from the tip at which the current contribution is still significant depends on the ratio $R_{mol\text{-}mol}/R_{mol\text{-}sub}$. When this ratio is large there is no or only small lateral transport since $\frac{V}{R_{mol-sub}} >> \sum_{n=1}^{N} 2\frac{V}{R_{mol-sub} + nR_{mol-mol}}$.

Because the current does not spread through the island the tip-sample current does not depend on the island size (fig.S3p and q). On the other hand, when the ratio $R_{mol\text{-}mol}/R_{mol\text{-}sub}$ is small lateral transport is significant. In the extreme case the current contribution comes from the entire island *width* for the 1D case (figS3k) and for the entire *area* for the 2D case (fig.S3m) and therefore scales with the island dimensions.

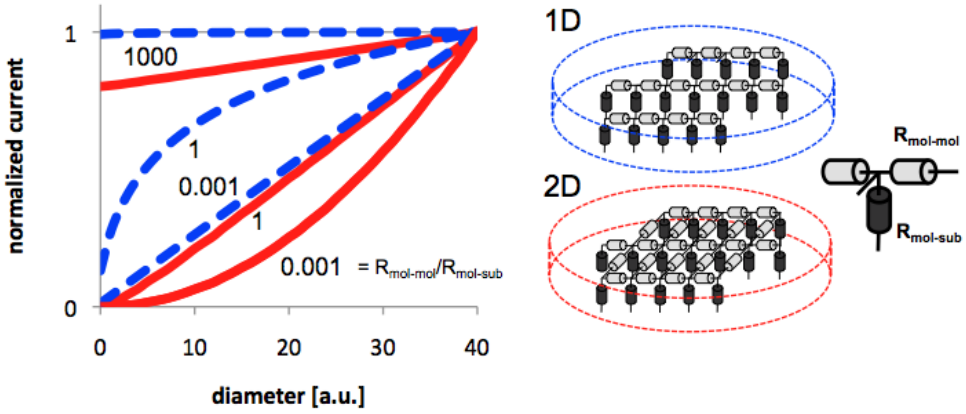


**Figure S2.** Calculated normalized current as function of the diameter of a circular shape resistor network consisting of (dashed blue) uncoupled arrays of resistors representing 1D conduction and (solid red) a square lattice of resistors representing 2D isotropic conduction. The current is shown for various ratios of $R_{mol\text{-}mol}$:$R_{mol\text{-}sub}$.

We calculated the current level at the center of a circular island as function of the island diameter using a square resistor network for various values of $R_{mol\text{-}mol}$ /$R_{mol\text{-}sub}$. Figure S2 shows linear scaling of the current with diameter (=length) of the network in 1D is only obtained when $R_{mol\text{-}mol} << R_{mol\text{-}sub}$. For the 2D case quadratic scaling is obtained in this case and linear scaling is only found when $R_{mol-sub} \approx R_{mol-mol}$. When we approximated the island shape in the experiments by a circular shape we observed a linear dependence on the diameter (fig. 3 of main text).
The ratios $R_{mol-sub} : R_{mol-mol}$, which led to the linear dependence for 1D and 2D respectively, show distinctive gradients in the calculated current maps (fig.S3 c and f). For 1D there is no gradient in the direction along the resistor arrays. Because the current depends on the length of the array, the current is lower for smaller widths resulting in a gradient in the perpendicular direction (fig.S3k and l). For the 2D case gradients exist when the area contributing to the current approaches the island edge (fig.S3o).

We used a similar resistor network model to calculate the current variations for a characteristic, simplified island shape consisting of a rectangular main body and a triangular protrusion representing a finger-like domain (Figure S4). Instead of using 1D arrays of resistors or a 2D isotropic network we use two separate resistors to represent the molecule-to-molecule resistance: $R_{mol-mol,a}$ in the **a** direction and $R_{mol-mol,b}$ in the perpendicular **b** direction. In figure 4a and b of the main text we show the results for the two situations, which led to a linear size dependence of the current, i.e. isotropic conduction with [$R_{mol-sub} \approx R_{mol-mol,a,b}$ and $R_{mol-mol,a} = R_{mol-mol,b}$ ], and anisotropic nearly-1D conduction with [$R_{mol-sub} \approx R_{mol-mol,a} >> R_{mol-mol,b}$]. These current images were calculated for each tip position by integration over all current paths contributing to the current. The calculated current paths contributing to the total current for one single pixel contact point (the CAFM tip position) are shown in figure S4 a-c. The isotropic conduction paths are a function of the distance away from the tip position. For the anisotropic case there is nearly no distance dependence in the **b** direction and a strong decrease in the **a** direction. The entire width in the **b** direction contributes to the tip-sample current.

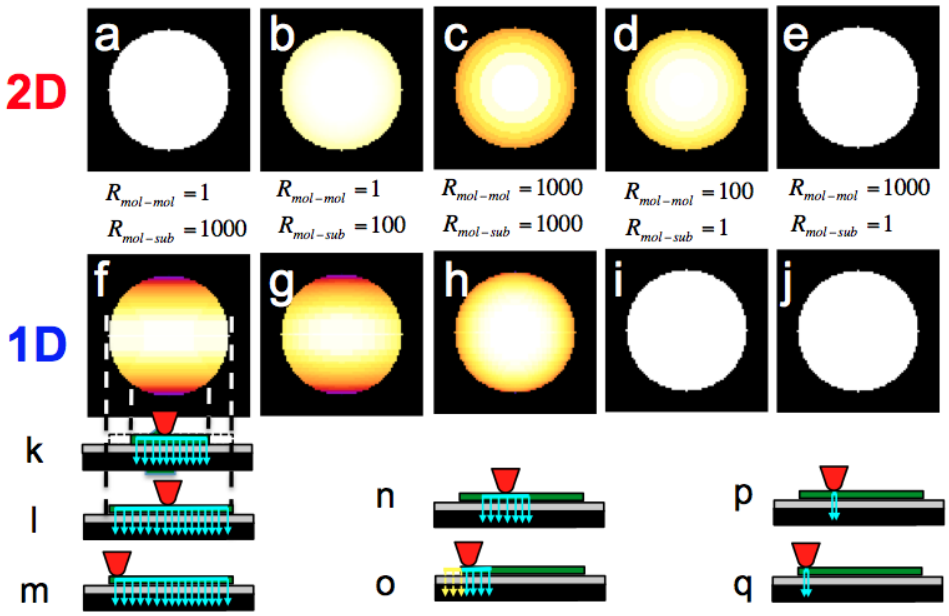


**Figure S3.** Current maps calculated for various $R_{mol\text{-}mol}$:$R_{mol\text{-}sub}$ ratios. (a-e) for a circular island containing a 2D resistor network. (f-j) for a 1D resistor network. (k,l) For the 1D case and a small molecule to molecule resistance the current flows through the entire array and depends on the length of the resistor array and therefore on the local width of the circular island. (m) For the 2D case and small molecule to molecule resistance the current flows through the entire resistor network, irrespective of the position of the tip contact. (n,o) For both 1D and 2D: when there is an appreciable molecule to molecule resistance current flow laterally through the network is limited. For contact locations at the center of the island the current is uniform, however the current level is reduced and a gradient exists. (p,q) For 1D and 2D: when the molecule to molecule resistance is large the lateral contribution of the network is small leading to a uniform current map, with only gradients at the very edge of the network (too small to observe).

Current images for various anisotropy ratios between the molecule-to-molecule resistance, i.e. for various $R_{mol-mol,a} : R_{mol-mol,b}$ and fixed $R_{mol-sub}$, are shown in fig.S4e-h. The most striking, but not surprising, difference between the current maps of fig.S4 e and h is the gradient in the current level. For the isotropic case the gradients are small and isotropic and for the anisotropic case no gradients exist in the **b** direction and strong gradients exists in the **a** direction. When we compare the calculated current images to the experimental CAFM images (an example is given in figure S4d) we find that there is best agreement with anisotropic conduction. In particular the large gradient at the position where finger-like protrusions connect to the main body of an island shows strong resemblance. The agreement between figure e and f suggests that there is no or little current flowing in the **a** direction and the current only depends of the width in the **b** direction.

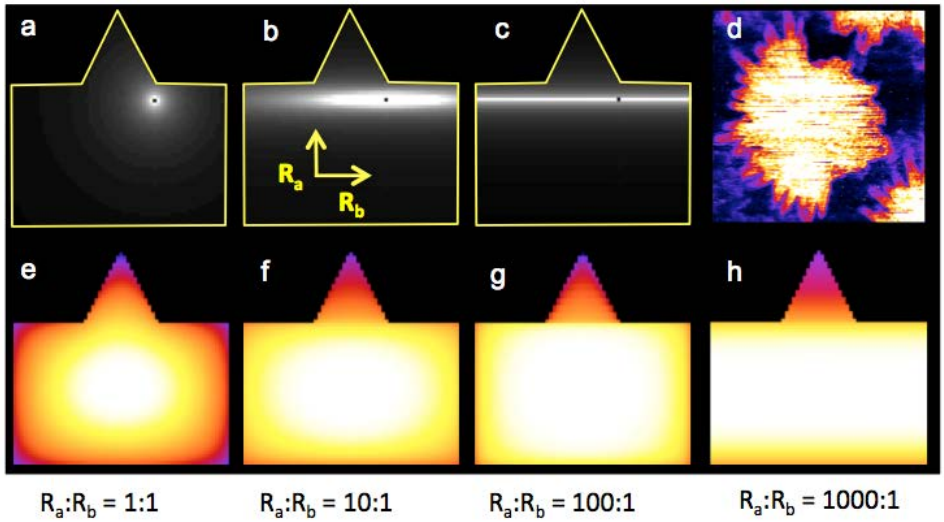


**Figure S4**. Current paths contributing to the total current for a single contact point (pixel) represented in grey scale (a) for isotropic conduction ($R_{mol\text{-}sub}$=$R_{mol\text{-}mol,a}$=$R_{mol\text{-}mol,b}$) for (b, c) anisotropic conduction ($R_{mol\text{-}sub}$≈$R_{mol\text{-}mol,a}$>>$R_{mol\text{-}mol,b}$). By integrating all current paths for each contact point pixel (CAFM tip position) we calculated the current maps of fig.4a and b in the main text. (d) Experimental CAFM current map showing a characteristic gradient, which is best reproduced by an anisotropic resistor network. (e)-(h) Current maps for a fixed $R_{mol\text{-}sub}$ and various anisotropy ratios $R_{mol,mol,a}$:$R_{mol,mol,b}$. The resistor network is defined in fig.4c of the main text.

**Current vs width in b direction**

When we plot the experimental current level for several finger-like protrusions as function of their local width we indeed find a linear dependence, shown as blue filled circles in fig.3b of the main text. These data were obtained from the current map shown in fig.S5a. The schematic in figure S5b illustrates that the width in the **b** direction may include grain/domain boundaries. The anisotropy is therefore mixed with conduction through these boundaries. The preparation of the D5TBA islands did not lead to single domain islands with sufficient spread in the **a** and **b** aspect ratios to allow a pure analysis of the conduction anisotropy. The D5TBA islands analyzed here always consisted of several domains separated by boundaries.

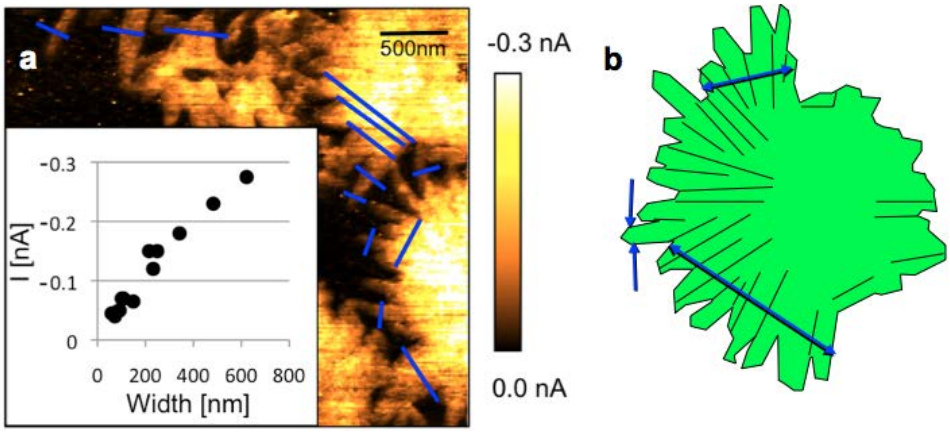


**Figure S5.** (a) Current-sensing AFM image of a D5TBA monolayer on a $SiO_2$/Sip+ substrate at $V_{sample}$= -2.0V and (inset) current as function of local width.. Blue lines indicate cross sections where the local width and current were measured for the plot of the inset and fig3b (the blue filled circles). (b) Schematic of the D5TBA island structure with blue arrows indicating the local widths in the **b** direction of the molecular lattice.

**Electronic structure calculations**

Room temperature atomic structures were obtained by taking a snapshot from the room temperature molecular dynamics simulation. The top 10 HOMO wavefunctions were calculated for 10 different room temperature molecular dynamics snapshots. Isosurfaces displayed in fig.4d show that molecular orbitals are strongly localized. Carrier hopping is likely the dominant transport mechanism in D5TBA LB monolayers.

*Anisotropy of hopping probabilities*

We estimate the hopping probability (which is linearly related to carrier mobility[1]) between the states *k* and *m* as being proportional to the square of the wavefunction moduli overlap

$$W_{km} \propto M_{km}^2 = \left[\int \left|\psi^{(k)}(\mathbf{r})\right|\left|\psi^{(m)}(\mathbf{r})\right| d^3\mathbf{r}\right]^2$$

where $\psi^{(k)}$ and $\psi^{(m)}$ are the wavefunctions for the realistic room temperature atomic structure (not the ideal crystal one) obtained as a snapshot from molecular dynamics simulation (some of these wavefunctions are shown in Fig. 4d which demonstrates that these are well localized). In our recent work [2], we have shown that such overlap integral approximates very well the full hopping matrix calculated by taking into account the electron-phonon interaction.

Next, we estimate the carrier diffusion constant using the following approach. The change of carrier *x*-coordinate after *n* carrier hops taking place during time *t* is

$$\Delta x = \Delta x_1 + \Delta x_2 + \ldots + \Delta x_n ,$$

where $\Delta x_i$ is the change of *x*-coordinate in the *i*-th time interval $\Delta t_i$. For uncorrelated carrier hops, it follows that

$$\left\langle (\Delta x)^2 \right\rangle = \left\langle (\Delta x_1)^2 \right\rangle + \left\langle (\Delta x_2)^2 \right\rangle + \mathsf{K} + \left\langle (\Delta x_n)^2 \right\rangle .$$

The diffusion constant in the *x*-direction is by definition

$$D_x = \frac{\left\langle (\Delta x)^2 \right\rangle}{t} .$$

Consider the i-th carrier hop within the time step $\Delta t_i$ from state k to all possible state m, we have the average distance square within this time step as:

$$\left\langle (\Delta x_i)^2 \right\rangle = \sum_m (x_k - x_m)^2 W_{km} \Delta t_i ,$$

Note, this angle bracket average includes case where no hopping has happened within $\Delta t_i$, and $W_{km}\Delta t_i$ is the probability that the carrier will hop to state *m*. If we further take an average over the initial state k (e.g., using a Boltzmann distribution, which is the initial state k distribution in a random walk), we will have

$$\left\langle (\Delta x_i)^2 \right\rangle = \frac{\sum_k f(k) \sum_m (x_k - x_m)^2 W_{km}}{\sum_k f(k)} \Delta t_i = D_x^* \Delta t_i .$$

Here f(k) is the Boltzmann distribution of state k depending on its eigenenergy.

---

[1] V. Coropceanu, J. Cornil, D. A. da Silva Fihlo, Y. Olivier, R. Silbey, J. L. Bredas, *Chem. Mater.* **2007**, 107, 926

[2] N. Vukmirovic and L.-W. Wang, arXiv:1005.1964v1.

Plug this into the above equation, and note that $t = \sum_i \Delta t_i$ , then we have $D_x = D_x^*$, and

$$D_x \propto \left\langle \left(x_k - x_m\right)^2 M_{km}{}^2 \right\rangle$$

The above expression can be generalized to an arbitrary direction $(\cos\alpha, \sin\alpha)$ other than *x* as

$$D_x \propto \left\langle [\left(x_k - x_m\right)\cos\alpha + (y_k - y_m)\sin\alpha]^2 M_{km}{}^2 \right\rangle$$

In Fig. 5b we plot the dependence of

$$g(\alpha) = \left\langle [\left(x_k - x_m\right)\cos\alpha + (y_k - y_m)\sin\alpha]^2 M_{km}{}^2 \right\rangle$$

on the direction $\alpha$. g has maximum at α = 90° (the [0,1] direction) and the minimum at α = 0° in the [1,0] direction. This implies that the [0,1] direction is the preferred direction for carrier diffusion. Since the diffusion constant and the mobility are linearly related by the Einstein relation, the same conclusion can be extended to carrier mobility.

**Kelvin probe force microscopy of trapped charges**

Figure 5 of the main article shows KPFM data, which we used to show that charge carriers can flow laterally and that these had opposite polarity for negative sample voltage (positive charge corresponding to holes) and positive sample voltage (negative charges corresponding to electrons). Figure S6 shows the complete set of KPFM images and a schematic illustration of the subsequent KPFM imaging and point contacting the D5TBA island. When the CAFM tip is brought in contact with the island a voltage is applied and holes/electrons are injected in the D5TBA island, which flow laterally through the island. A small fraction of the charge carriers is trapped either in the island or the underlying oxide. If we assume that the trapped charge is proportional to the local current density during contact charge injection, then the KPFM image represent the current profiles during the current flow. The KPFM images however do not reflect the conduction anisotropy discussed above.

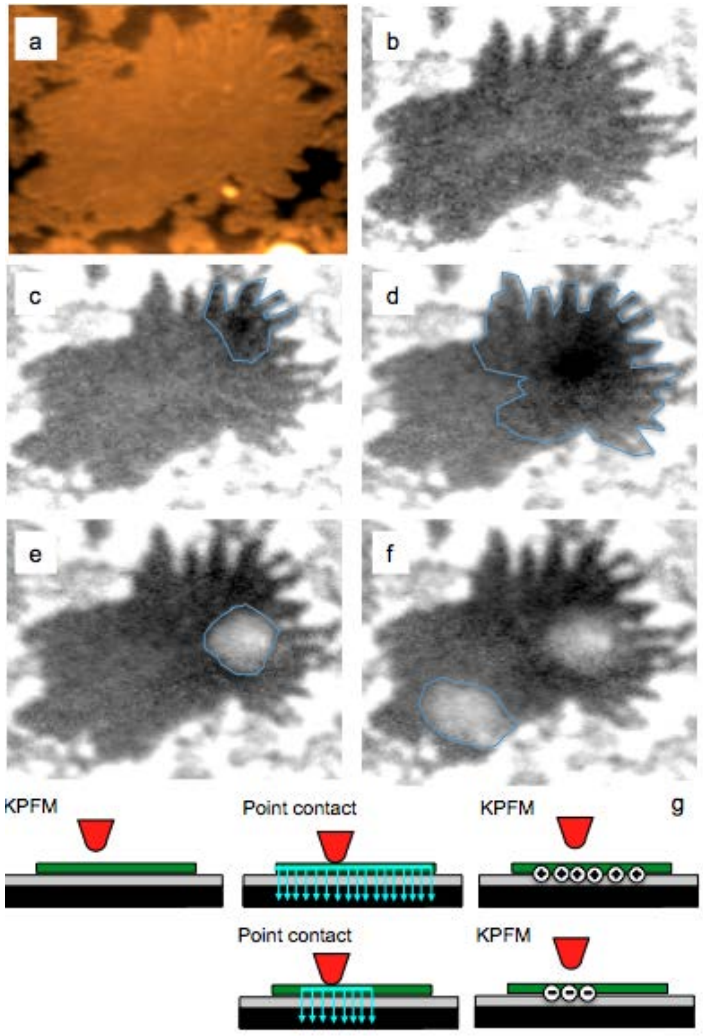


**Figure S6.** (a) NC-AFM topography. (b-f) Contact potential different images obtained by KPFM. (c,d) KPFM images obtained after point contacting the D5TBA island at positive sample voltage. This resulted in a lowering of the CPD (indicative of trapped positive charge) well outside of the point contact. (e,f) Same after point contact at negative sample voltage, which resulted in an increase of the CPD (trapped negative charge) again well outside of the point contact area. (g) Scheme of the sequence of KPFM and point contact measurements.

**Current maps as function of sample voltage**

Figure S7 shows the current images at various sample voltages, which were used for the IV curves of fig.S7c and figure 6 of the main text; the color scales were adjusted for each image for best contrast. Figure S7a and b show the topography and lateral force images respectively. The current image at -0.5V shows that the current level on each island is nearly uniform (e.g. for largest island at $V_{sample}$=-0.5V: average current <I>=-0.028nA, standard deviation σ=0.01nA; at $V_{sample}$=-2.5V: <I>=0.210nA, σ=0.07nA) and shows no internal structure except for the finger-shaped protrusions, which have a reduced current due to their smaller width (see above). All current images in the range of -0.5 to -3.0V look identical, but with different, increasing magnitude of the current level scale. This trend is consistent with lateral transport of holes injected into the HOMO, which starts at $V_{sample}$=-0.5V as soon as the HOMO becomes resonant with the Fermi level in the tip.

At positive sample voltage the spatial variations of current are different. The current levels are not uniform within an island and local spike-like variations can be observed with lateral

dimensions of 10-60nm (for largest island at $V_{sample}$=+2.5V: <I>=-0.031nA, σ=0.054nA). These variations in the current are reproducibly found at the same location on the islands, but they did not correlate with structural variations of the islands observed in the friction images, e.g. domain boundaries. We believe that these variations are visible because of a reduced lateral conduction for electrons (i.e. at positive sample voltage). The variations in the current reflect: (1) spatial variations in the tip-molecule contact; (2) the length scale of the lateral transport; or (3) variations in the local resistance in the $SiO_2$ substrate. Since variations in the tip-molecule contact are expected to be the same for positive and negative sample voltages we conclude that (2) or (3) are responsible for the observed variations. Also (3) implies a reduced lateral conduction, because lateral conduction in the islands obscures variations in the local resistance of the oxide layer below the island, as is the case for negative sample voltages.

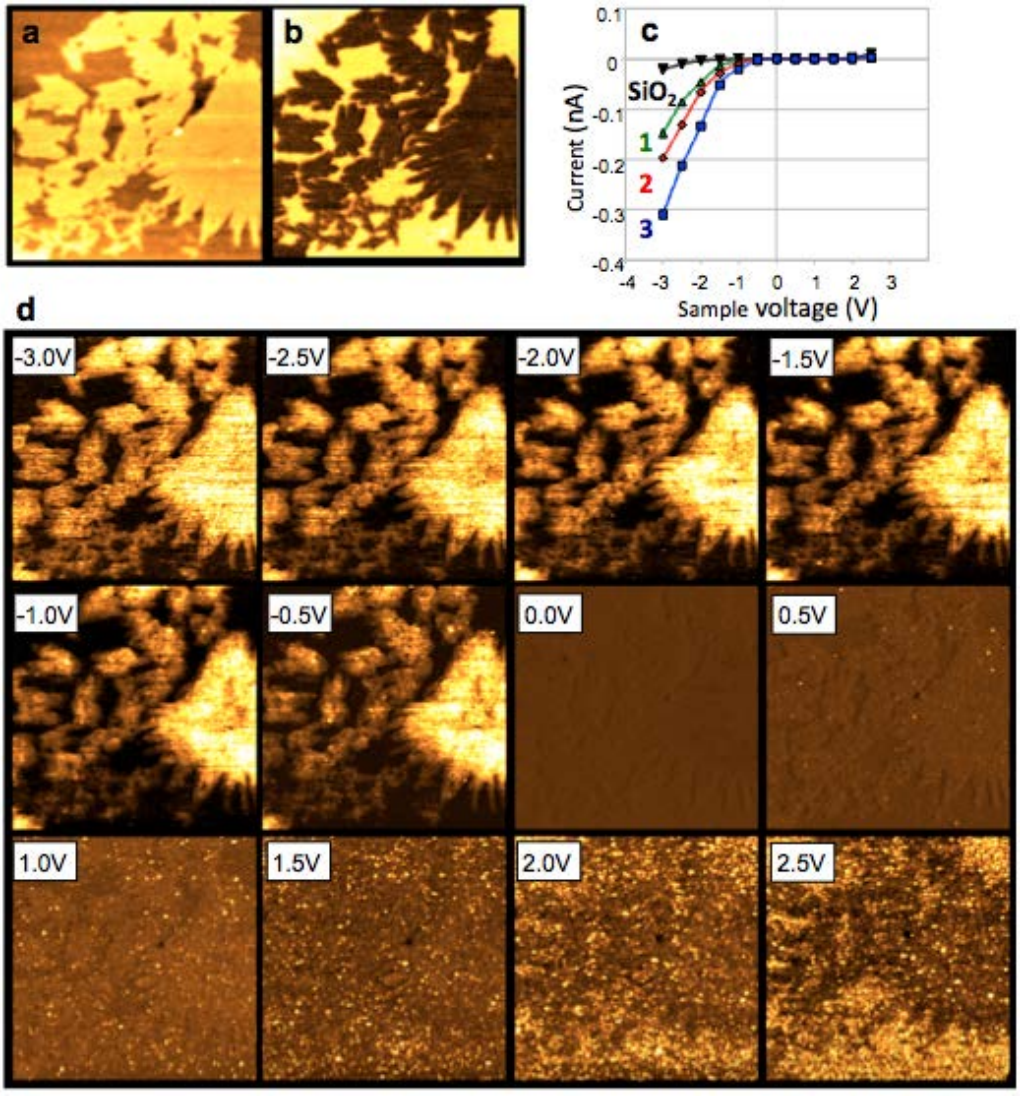


**Figure S7**. (a) AFM topographic image of D5TBA island on $SiO_2$/Si and (b) lateral force (friction) image. (c) Current-voltage characteristics extracted from CAFM current maps. (d) CAFM current maps from which the IV curves in (c) were extracted. At each sample voltage the color scale of the current image is rescaled for maximum contrast. In all cases the brightest color is assigned to the highest absolute current.